Correlation analysis of frustrated tunneling ionization

I. A. Ivanov [1,2,*] A. S. Kheifets [2,†] and Kyung Taec Kim [1,3,‡]
[1] *Center for Relativistic Laser Science, Institute for Basic Science, Gwangju 61005, Republic of Korea*
[2] *Research School of Physics, Australian National University, Canberra ACT 2601, Australia*
[3] *Department of Physics and Photon Science, GIST, Gwangju 61005, Korea*

(Received 11 January 2023; revised 26 February 2023; accepted 30 March 2023; published 7 April 2023)

We visualize frustrated tunneling ionization (FTI) using the correlation function analysis outlined in our preceding works [I. Ivanov and K. T. Kim, J. Phys. B **55**, 055001 (2022); Sci. Rep. **12**, 19533 (2022)]. We apply this technique to the hydrogen atom subjected to a strong laser field. Our analysis supports the basic premises of the theory of FTI and demonstrates its sensitive dependence on the laser pulse duration and carrier envelope phase.

DOI: 10.1103/PhysRevA.107.043106

I. INTRODUCTION

Interaction of an atom with a strong laser field can lead to population of highly excited Rydberg states. This process was realized to be behind stabilization of atomic ionization in an intense laser field. Because of the lack of adequate lasers to study ground states of single-active-electron atoms, the early experiments have been performed on low-lying Rydberg states (see Gavrila [1] for a comprehensive review). The situation has changed with the advent of superintense lasers. Nubbemeyer *et al.* [2] demonstrated experimentally an effect of strong-field tunneling without ionization on the ground state of helium. They termed this effect a frustrated tunneling ionization (FTI). At a laser intensity of 1×10^{15} W/cm^2, Nubbemeyer *et al.* [2] observed a population of Rydberg states with $n = 8$ and higher. This discovery has prompted a stream of subsequent experimental and theoretical works (see, e.g., [3–13]). Besides the fundamental interest, the creation of highly excited metastable states in FTI has a potential for various applications [14–17]. In addition, these states can decay to the ground state and produce coherent extreme ultraviolet (EUV) radiation. Such radiation termed below-threshold harmonic generation [9,18] or “FTI emission” [19,20] will be valuable for EUV imaging [21].

The mechanism of FTI is best understood by comparing it with another strong-field ionization phenomenon, high-order harmonic generation (HHG) [see Fig. 1(a) in Yun *et al.* [19] for pictorial illustration]. The photoelectrons that tunnel out after the peak of the laser field recombine, after returning to the parent ion, to the ground state leading to HHG. The FTI electrons tunnel out during the peak of the laser field, oscillate in the field near the parent ion, and then recombine to highly excited Rydberg states.

Such a mechanism of FTI has been confirmed by various modelings employing the strong-field approximation (SFA) [20] or classical trajectory Monte Carlo (CTMC) simulations [7,12,22]. In the present paper, we offer yet another means to visualize the FTI process. We present a correlation analysis of FTI based on our preceding works [23,24]. Such an approach allows us to solve the following difficult problem one encounters trying to extract information about temporal development of ionization or FTI processes for times inside the laser pulse. Quantum mechanics provides us with a total wave function describing evolution of the system in the laser field. It is not quite clear how to unambiguously single out the part of the wave function describing ionized or FTI electrons from this total wave function for the moments of time inside the laser pulse, when the wave packets describing FTI or ionized electrons and the initial ground state are not yet spatially separated. Such a resolution of the total wave function in several components lies at the heart of the well-known SFA and Perelomov-Popov-Terent’ev (PPT) approaches [25]. One should note, however, that the resolution of the total wave function used in these theories is achieved at the price of omitting certain terms from the total wave function and is not quite rigorous, therefore. This omission, in particular, leads to the well-known lack of the gauge invariance of the SFA or PPT approaches [25].

A more detailed description of this issue can be found in our preceding paper [24]. In that work we described a procedure based on the analysis of correlations which allows us to single out the wave packet describing ionized electrons and applied this procedure to study strong-field ionization process. In the present paper we apply this approach to analyze the FTI process. This analysis, as we shall see, paints, in the most graphical way, the picture of FTI as it develops in real time. We apply this technique to the hydrogen atom subjected to a strong laser field. This way we visualize the birthplace and the trajectory of the FTI electrons. Our analysis supports the basic premises of current understanding of the FTI and demonstrates its sensitive dependence on the laser pulse duration and carrier envelope phase (CEP).

The rest of the paper is organized as follows. In Sec. II we introduce the correlation function and explore its physical meaning and properties. In Sec. III we present and interpret

*igorivanov@ibs.re.kr
†A.Kheifets@anu.edu.au
‡kyungtaec@gist.ac.kr

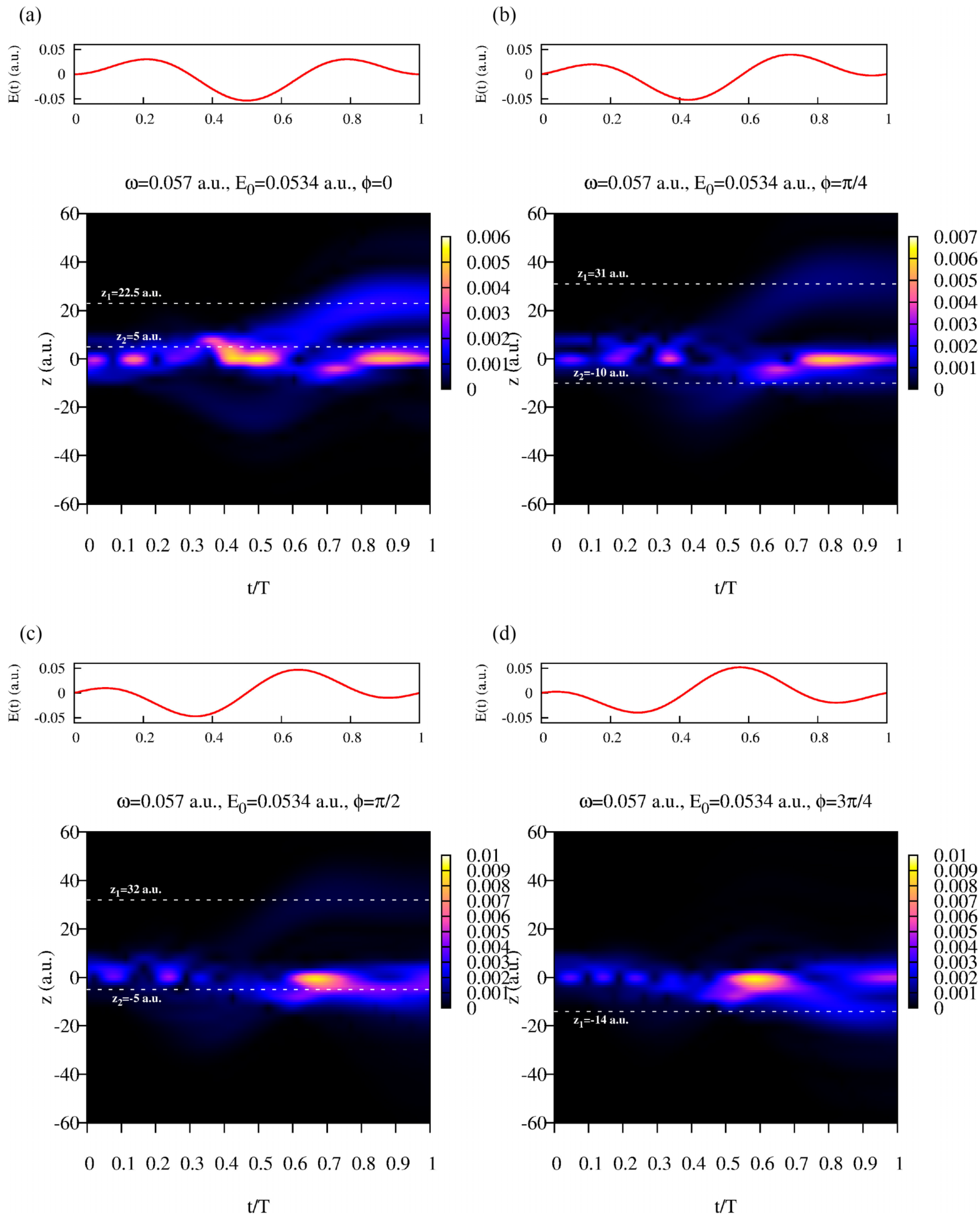

FIG. 1. Pulse shapes and magnitudes $|\tilde{C}(z_0, t; \mathcal{R}, T_1)|$ of the normalized correlation function (8) for single cycle pulses with different CEPs. Time is measured in units of an optical cycle $T = 2\pi/\omega$. White dashed lines show z coordinates of the crests of the FTI wave packets at the end of the pulse.

our main numerical results. We conclude in Sec. IV by summarizing our findings and outlining the further prospects of the present paper.

II. THEORY

A. The correlation function

To calculate the correlation function we use a procedure similar to the one we used previously in [23,24] to study correlations between an electron's coordinate and velocity in the strong-field ionization process. We recapitulate briefly the procedure, indicating the modifications we have to make to be able to study the FTI process.

We consider the hydrogen atom interacting with a linearly polarized laser pulse defined in terms of the vector potential: $\boldsymbol{E}(t) = -\frac{\partial \boldsymbol{A}(t)}{\partial t}$, where

$$\boldsymbol{A}(t) = -\hat{\boldsymbol{e}}_z \frac{E_0}{\omega} \sin^2\left(\frac{\pi t}{T_1}\right) \sin(\omega t + \phi), \tag{1}$$

where $T_1 = N_c T$ is the total pulse duration and $T = 2\pi/\omega$ is the optical cycle (OC) corresponding to the base frequency ω. For the majority of the calculations reported below we will use a single cycle pulse with $N_c = 1$. We will also present some results for the multicycle pulses with $N_c = 2$–4. In Eq. (1) E_0 is the peak field strength of the pulse, and ϕ is its CEP.

The evolution of the system is described by the time-dependent Schrödinger equation (TDSE):

$$i\frac{\partial \Psi(\boldsymbol{r},t)}{\partial t} = [\hat{H}_{\text{atom}} + \hat{H}_{\text{int}}(t)]\Psi(\boldsymbol{r},t). \tag{2}$$

In Eq. (2) $H_{\text{atom}} = \frac{\hat{p}^2}{2} - \frac{1}{r}$ is the field-free atomic Hamiltonian and $\hat{H}_{\text{int}}(t)$ is the interaction Hamiltonian describing atom-field interaction which we take in the length gauge form:

$$\hat{H}_{\text{int}}(\boldsymbol{r},t) = \boldsymbol{r}\cdot\boldsymbol{E}(t), \tag{3}$$

where $\boldsymbol{E}(t)$ is the electric field of the pulse.

The goal of the present paper is to study the history of the FTI electrons, i.e., the history of the electrons ending in a Rydberg state at the end of the laser pulse. An appropriate tool for this paper will be, as we shall see below, the correlation function describing correlations between two quantum-mechanical operators: a projector $\hat{P}_{\mathcal{R}}$ on the manifold of the atomic Rydberg states $\mathcal{R}$, and a projector $\hat{P}_{z_0}$, projecting the coordinate wave function on a region of Ω_{z_0} of the electron's coordinate space centered around the point $\boldsymbol{r} = (0,0,z_0)$. We will characterize the manifold $\mathcal{R}$ of the hydrogen Rydberg states as a set of all the atomic levels with principal quantum number $n \geqslant 2$. The projection operator $\hat{P}_{z_0}$ has been defined in the calculations as $\hat{P}_{z_0} = |\phi_{z_0}(\boldsymbol{r})\rangle\langle\phi_{z_0}(\boldsymbol{r})|$. For $|\phi_{z_0}(\boldsymbol{r})\rangle$ we use the Gaussian form: $\phi_{z_0}(\boldsymbol{r}) = Ne^{-a(\boldsymbol{r}-\boldsymbol{e}_z z_0)^2}$, where N is the normalization factor and we use the value $a = 4\ln 2$ for the parameter a. This parameter defines the "resolution" with which we can look at the electron's coordinates, and it is approximately 1 a.u. of length for the choice of the parameter a we made.

We will first provide a definition of the correlation function, and later explain its relevance to the problem we are considering. We are interested in a two-time correlation function, describing the correlation between the two events: detection of the electron in a Rydberg state at the moment $t = T_1$ corresponding to the end of the pulse, and finding the electron in a region Ω_{z_0} at time t inside the laser pulse. Such two-time correlation functions are most naturally introduced in the Heisenberg picture of quantum mechanics [26–29]. We use, therefore, Heisenberg representation for both projection operators $\hat{P}_{\mathcal{R}}$ and $\hat{P}_{z_0}$:

$$\begin{aligned}\hat{P}^H_{\mathcal{R}}(t) &= \hat{U}(0,t)\hat{P}_{\mathcal{R}}\hat{U}(t,0),\\ \hat{P}^H_{z_0}(t) &= \hat{U}(0,t)\hat{P}_{z_0}\hat{U}(t,0),\end{aligned} \tag{4}$$

where $\hat{U}(t,0)$ is the evolution operator, describing the quantum evolution of the system. The two-time correlation function describing the correlations between the two events—finding the electron in a Rydberg state belonging to the manifold $\mathcal{R}$ at the moment $t = T_1$ corresponding to the end of the pulse, and finding the electron in a region Ω_{z_0} at time t inside the laser pulse—can now be defined as

$$C(z_0,t;\mathcal{R},T_1) = \langle\phi_0|\hat{P}^H_{z_0}(t)\hat{P}^H_{\mathcal{R}}(T_1)|\phi_0\rangle, \tag{5}$$

where ϕ_0 is the initial state of the system which we assume to be the ground state of the hydrogen atom. Once this formula is obtained, we can go back to the Schrödinger representation which is, of course, better suited for the practical calculations. Using the transformation equations (4) we obtain

$$C(z_0,t;\mathcal{R},T_1) = \langle\Psi(t)|\hat{P}_{z_0}\hat{U}(t,T_1)\hat{P}_{\mathcal{R}}|\Psi(T_1)\rangle, \tag{6}$$

where P_{z_0} and $\hat{P}_{\mathcal{R}}$ are the time-independent projection operators of the Schrödinger picture, and $|\Psi(t)\rangle = \hat{U}(t,0)|\phi_0\rangle$ is the state vector describing the system in the Schrödinger picture at the moment of time t. To actually compute the correlation function in Eq. (6) we proceed as follows. We propagate the TDSE (2) on the interval $(0,T_1)$ of the laser pulse duration starting with an initial atomic state $|\Psi(0)\rangle = |\phi_0\rangle$, thus obtaining the state vector $|\Psi(T_1)\rangle$ describing the system at the end of the pulse. Acting with the Schrödinger operator $\hat{P}_{\mathcal{R}}$ on this state vector we obtain a vector $|\Psi_1(T_1)\rangle = \hat{P}_{\mathcal{R}}|\Psi(T_1)\rangle$. We then propagate $|\Psi_1(T_1)\rangle$ back in time on the interval (t,T_1) obtaining the vector $|\Psi_1(t)\rangle$, from which we obtain $|\Psi_2(t)\rangle = \hat{P}_{z_0}|\Psi_1(t)\rangle$. The correlation function (6) can then be found by projecting $|\Psi_2(t)\rangle$ on the state vector $|\Psi(t)\rangle$.

The TDSE was solved numerically using the procedure we tested and described in detail in [30–32]. The procedure relies on representing the coordinate wave function as a series in spherical harmonics with quantization axis along the pulse polarization direction. Spherical harmonics with orders up to $L_{\max} = 50$ were used. The radial variable is treated by discretizing the TDSE on a grid with the step size $\delta r = 0.05$ a.u. in a box of the size $R_{\max} = 200$ a.u. Necessary checks were performed to ensure that for these values of the parameters $L_{\max}$ and $R_{\max}$ convergence of the calculations has been achieved. The solution of the three-dimensional TDSE was propagated both forward and backward in time using the matrix iteration method [33].

B. Physical meaning of the correlation function

It is worthwhile to discuss expression (6) for the correlation function in more detail to understand what information we can hope to extract from it. Let us first consider a (somewhat unrealistic) situation when the Heisenberg projection operators $\hat{P}^H_{z_0}(t)$ and $\hat{P}^H_{\mathcal{R}}(T_1)$ in Eq. (5) commute. Their product in Eq. (5) is then again a Hermitian projection operator. This Hermitian projection operator is positively defined, and its positive and real expectation value in Eq. (5) can be regarded as an expression for the joint probability of the occurrence of two events: detection of the electron in a Rydberg state belonging to the manifold $\mathcal{R}$ at the moment $t = T_1$ corresponding to the end of the pulse, and finding the electron in a region Ω_{z_0} at time t inside the laser pulse. This interpretation is a natural generalization, for the case of different times, of the well-known fact that commuting Hermitian operators have common system of eigenfunctions, and it provides a basis for the introduction of the notion of the joint probability in quantum mechanics [34–36]. If the operators in the definition of the correlation function (5) only approximately commute, that is, their commutator is in some sense small, the correlation function can still be interpreted as a joint probability distribution since in this case the imaginary part of it is small and it is almost everywhere positive. We used this interpretation of the correlation function in [24] to study the formation of the lateral velocity distribution in tunneling ionization. For the pair of the operators we consider presently, $\hat{P}^H_{z_0}(t)$ and $\hat{P}^H_{\mathcal{R}}(T_1)$, their commutator does not vanish even approximately, the correlation function (5) is inherently complex valued, and we cannot assign to it the meaning of the joint probability. However, by its very definition, the correlation function still provides information about correlation of the two events: detecting the electron in a Rydberg state belonging to the manifold $\mathcal{R}$ at the moment $t = T_1$ corresponding to the end of the pulse, and finding the electron in a region Ω_{z_0} at time t inside the laser pulse. To see what information we can extract from this correlation function let us take a closer look at Eq. (6) for the correlation function. Let us assume that the wave packet Φ which at the end of the pulse ends in the manifold $\mathcal{R}$ of the Rydberg states is formed at the moment t_0 inside the laser pulse. The operator $\hat{P}_{\mathcal{R}}$ acting on the final-state wave function $\Psi(T_1)$ selects this wave packet $\Phi(T_1)$ from the total wave function of the system. Next, the evolution operator $\hat{U}(t, T_1)$ propagates it back in time till the time moment t giving us the wave packet $\Phi(t)$. The action of the projection operator $\hat{P}_{z_0}$ on this wave packet gives us a vector $\langle\phi_{z_0}|\Phi(t)\rangle|\phi_{z_0}\rangle$ with the Gaussian $|\phi_{z_0}\rangle$ we specified above. The correlation function (6) can, therefore, be written as

$$C(z_0, t; \mathcal{R}, T_1) = \langle\Psi(t)|\phi_{z_0}\rangle\langle\phi_{z_0}|\Phi(t)\rangle. \quad (7)$$

For the Gaussian choice of $|\phi_{z_0}\rangle$ the two factors on the right-hand side of Eq. (7) are the Weierstrass transforms [37] of the vector, $\Psi(t)$ is the total wave function of the system at time t, and $\Phi(t)$ is the wave packet which ends up in the manifold $\mathcal{R}$ of the Rydberg levels after the end of the pulse. The Weierstrass transform is often used in the image processing, and is, as can be seen from the definition, just a Gaussian "smoothing" of the original function. The factor $\langle\Psi(t)|\phi_{z_0}\rangle$ on the right-hand side of Eq. (7) is the Weierstrass transform of $\Psi(t)$. For not too high electric-field strengths we consider presently, when depletion of the ground state is small, this factor is concentrated in the region of small z_0. Knowing the correlation function for different z_0 and t allows us to obtain information about the more interesting second factor $\langle\phi_{z_0}|\Phi(t)\rangle$ which is just the Weierstrass transform of the FTI wave packet considered as a function of time t and coordinate z. This factor gives us information about the spatial development of the FTI wave packet in time. We divide, therefore, the correlation function (7) by the factor $\langle\Psi(t)|\phi_{z_0}\rangle$ and will concentrate below on the study of the normalized correlation function:

$$\tilde{C}(z_0, t; \mathcal{R}, T_1) = \frac{C(z_0, t; \mathcal{R}, T_1)}{\langle\Psi(t)|\phi_{z_0}\rangle}. \quad (8)$$

Results of this study are presented in the next section.

III. RESULTS AND DISCUSSION

A. Single cycle pulse: CEP dependence

As we discussed above, the normalized correlation function is closely related to the time-dependent Weierstrass transform of the FTI wave packet. The locations of the local absolute maxima of this function for fixed moments of time can be naturally interpreted as the instantaneous z coordinates of the crest of the FTI wave packet. Thus, a study of the curves in the (t, z) plane which the locations of the maxima follow in time can be used to visualize the FTI wave-packet trajectories.

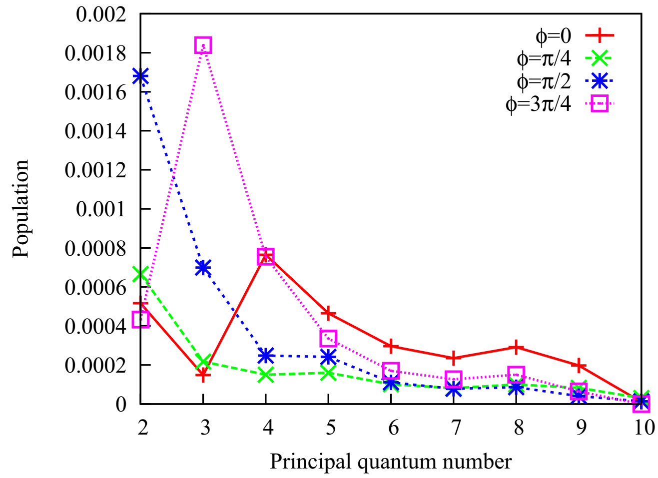

FIG. 2. Population of Rydberg levels for a single cycle pulse with peak field strength $E_0 = 0.0534$ a.u., base frequency $\omega = 0.057$ a.u., and different CEPs.

In Fig. 1 we present results of the calculation of the normalized correlation function (8) for a single cycle pulse with the peak field strength $E_0 = 0.0534$ a.u. and $\omega = 0.057$ a.u. with different values of the CEPs. The prominent maxima lying on the z axis near the maxima of the electric field of the pulses can be interpreted as instants and locations of the birth of the FTI wave packets. As one see from the figure, the FTI wave packets are born near the field maxima. This observation, which we made by using a purely quantum-mechanical reasoning, based on the study of the correlation function, agrees well with the CTMC analysis [7,12]. The plots shown in Fig. 1 allow us to follow the evolution of the FTI wave packets after the birth event. We can discern in Fig. 1 several sleeves in the patterns of $|\tilde{C}(z_0, t; \mathcal{R}, T_1)|$, located at various distances from the origin. The corresponding z values at the moment $t = T_1$ allow us to estimate which particular Rydberg states are occupied at the end of the pulse. We can use for this purpose the well-known formula for the average distance from the origin in an n, l state of the hydrogen atom [38]:

$$r(n, l) = [3n^2 - l(l+1)]/2. \quad (9)$$

The results of the Rydberg state populations at the end of the pulse are shown in Fig. 2 for different CEPs that we are considering. These results are obtained by first projecting the wave function at the end of the pulse on a corresponding hydrogen state with the pair of the quantum numbers (n, l). In this way we obtain a set of the probabilities $P(n, l)$, each $P(n, l)$ giving probability to find the electron in a Rydberg state (n, l) after the end of the pulse. By summing $P(n, l)$ over all l we obtain the results shown in Fig. 2. The average distance at which the wave packet corresponding to the Rydberg electrons with a given n may be found at the end of the pulse can be estimated as

$$\bar{r}_n = \frac{\sum_l P(n, l) r(n, l)}{\sum_l P(n, l)}. \quad (10)$$

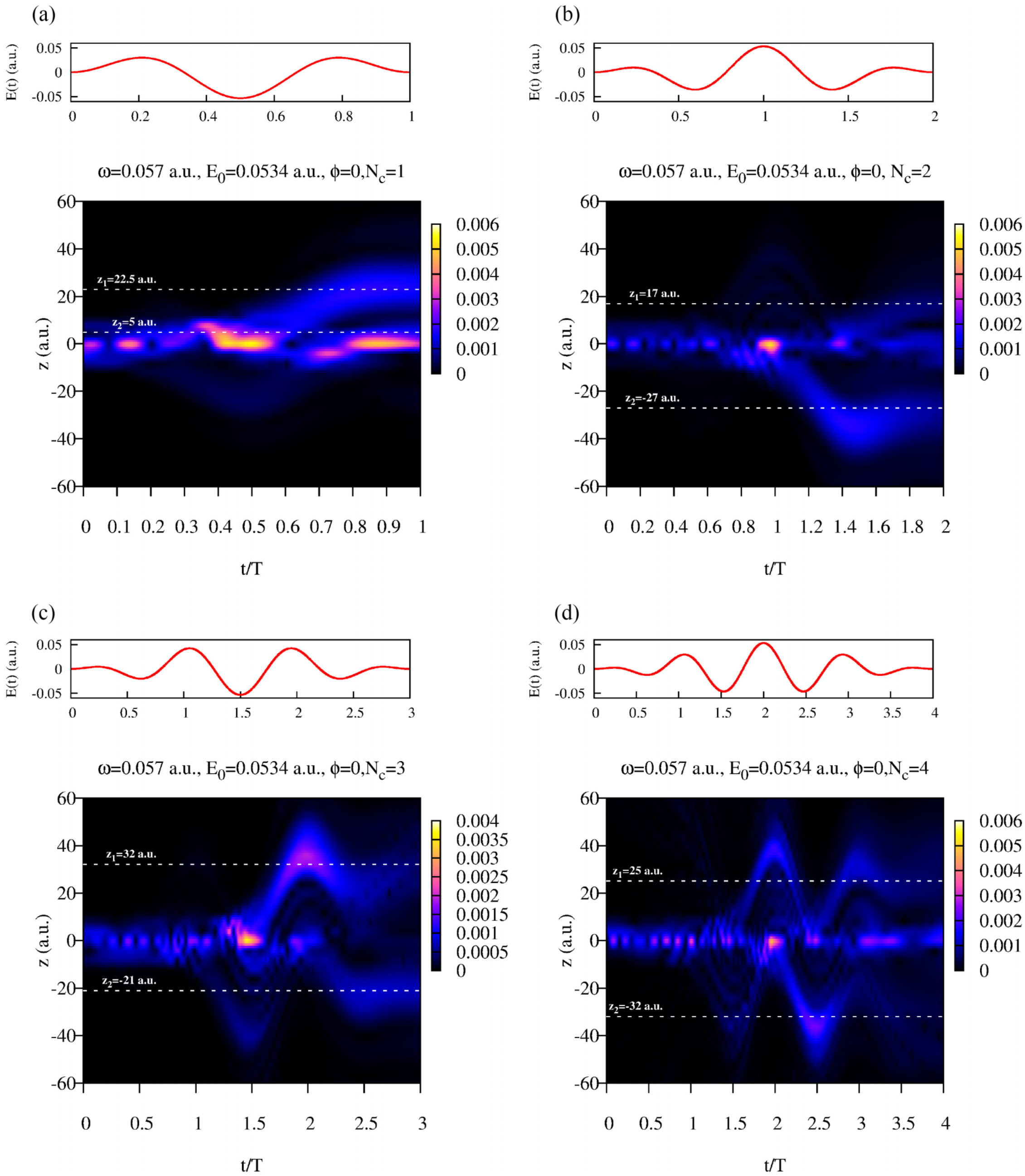

FIG. 3. Magnitude $|\tilde{C}(z_0, t; \mathcal{R}, T_1)|$ of the normalized correlation function (8) for multicycle pulses with number of cycles $N_c = 1$–4. Time is measured in units of an optical cycle $T = 2\pi/\omega$. White dashed lines show z coordinates of the crests of the FTI wave packets at the end of the pulse at $t = N_c T$.

We can see from Fig. 2 that for $\phi = 0$ the maximum population is attained for the Rydberg state submanifold with $n = 4$. The simple formula (10) gives $\hat{r}_n \approx 21.5$ a.u. for this case. On the other hand, Fig. 1(a) shows that for $\phi = 0$ there are two well-discernible wave-packet birth events near the local-field maxima at $t \approx 0.5T$ and $0.8T$. The crest of the wave packet born at $t \approx 0.5T$ terminates at the end of the pulse at the point $z \approx 22.5$ a.u. which is in very good agreement with the simple estimate of the average distance that we presented above using Eq. (10). The second sleeve in Fig. 1(a) which originates at $t \approx 0.8T$ has smaller z values at the end of the pulse and corresponds to the electrons trapped in the $n = 2$ Rydberg states which, as Fig. 2 shows, are also present with appreciable probability. For these electrons the simple estimate (10) gives an average distance of approximately 5 a.u. which again agrees with the results shown in Fig. 1(a). This difference in the final z values for the wave packets originating at different field maxima is probably related to the different spatial scales of the electron's motion for the electrons released at different peaks of the laser pulse. It was found in [2] that the maximum in the n distribution of the Rydberg level population in the FTI process scales with the strength of the electric field approximately as $n_{\max} \propto \sqrt{E_0}/\omega$. This simple qualitative dependence follows from the expression E_0/ω^2 for the electron's excursion radius and the quadratic n dependence of $r(n, l)$ in Eq. (9). We can use a similar line of arguments for the electrons released at different local peaks of the electric field. For such electrons the scales of the spatial motion are set by the effective electron excursion radii $E_{\rm eff}/\omega^2$ defined by an effective field strength on the interval of time between ionization moment and the end of the pulse. In the example shown in Fig. 1(a) we discussed above, this effective field strength and consequently the spatial motion scale would be smaller for the electrons released at $t \approx 0.8T$ than the spatial scale for the electrons ionized at $t \approx 0.5T$, leading to generally smaller average electron-ion distance and smaller n values for the Rydberg states populated at the end of the pulse.

Thus we see that the correlation function analysis we presented in Fig. 1 reproduces correctly the population of the Rydberg states obtained at the end of the pulse. More importantly, this analysis gives us a glimpse into the past history of the wave packets ending up in different Rydberg manifolds.

The correlation patterns for $\phi = \pi/4$ [Fig. 1(b)] and $\phi = \pi/2$ [Fig. 1(c)] also show the picture that is consistent with the final population distribution of the Rydberg states for these CEPs shown in Fig. 2. Figure 2 shows that the Rydberg state population in these cases is at maximum for the $n = 2$ manifold, which agrees with the picture we see in Fig. 1. Finally, for $\phi = 3\pi/4$ Fig. 2 shows that the population maximum at the end of the pulse is attained for the $n = 3$ Rydberg manifold with corresponding estimate $\bar{r}_n \approx 12$ a.u. for the average spatial size of this manifold obtained using Eq. (10). The correlation pattern in Fig. 1(d) tells us a similar story. We see formation of a distinct sleeve in the correlation pattern with the maximum intensity at about $z \approx -14$ a.u. at the end of the pulse. The correlation pattern, however, gives us more information than just the population distribution at the end of the pulse. It tells how this distribution evolved in time. In particular, we see in Fig. 1(d) that the FTI wave packet which ended in the $n = 3$ submanifold is born near the midpoint of the pulse, but unlike the case of the zero CEP in Fig. 1(a) it is born after the moment of the maximum field intensity.

B. Multicycle pulses

Figure 3 shows correlation patterns we obtain for multicycle pulses for the pulses (1) with $N_c = 1$–4, $E_0 = 0.0534$ a.u., $\omega = 0.057$ a.u., and zero CEP. The plots show that for the multicycle pulses several FTI wave packets are born, each at the instant of time near a local maximum field intensity. The distances from the parent ion at which these wave packets find themselves at the end of the pulse generally grow with the pulse duration. This observation is supported by the results for the Rydberg state population after the end of the pulse shown in Fig. 4, which were obtained by projecting the final-state wave function of the system of various Rydberg states. These results, in turn, agree with the observation made in [12] that an increasing pulse duration depletes lower-lying Rydberg states leading to the increase of the population of the higher-lying Rydberg levels. It was argued in [12] that the mechanism behind this depletion of low-lying Rydberg states is the electron's recollisions with a parent ion, which occur sooner for low-n states [12]. Once a critical number of optical cycles is exceeded, the electron can return to the parental ion, experience recollision, and acquire sufficient energy to get ionized. It was shown in [12] that this mechanism

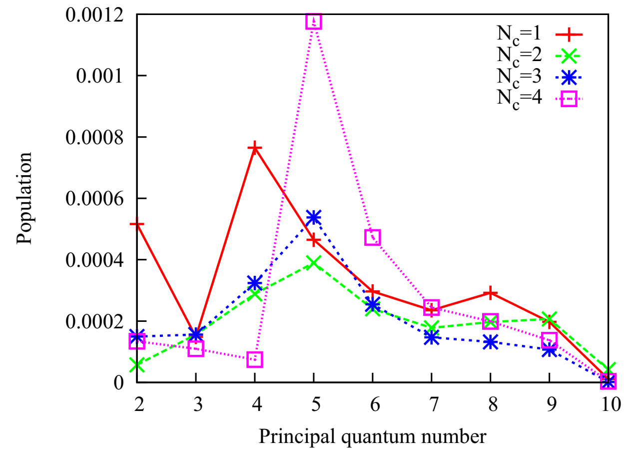

FIG. 4. Population of Rydberg levels for multicycle pulses with $E_0 = 0.0534$ a.u., $\omega = 0.057$ a.u., and different number of cycles.

becomes quite general, and acts independently of the particular pulse parameters for sufficiently long pulses, with some possible deviations occurring for very small pulse durations [12]. We do see such deviations in Figs. 3 and 4; in particular, the populations of the low-lying Rydberg states with $n \leqslant 4$ are higher for $N_c = 3$ than for $N_c = 2$. Nevertheless, the most notable feature seen in Fig. 4, the steady increase of the population of the $n = 5$ states with growing pulse duration for $N_c \geqslant 2$, agrees with the trend observed in [12]. This trend is also visible from the correlation pattern in Fig. 3. The FTI wave-packet trajectories in Figs. 3(b)–3(d) terminate at the end of the pulse at the distance $|z| \approx 30$ a.u. from the parent ion, which agrees well with the average spatial size of the low angular momentum states of the $n = 5$ manifold given by Eq. (9). Correlation patterns for the multicycle pulses in Fig. 3 agree, therefore, with the results in the literature as far as the Rydberg level population after the end of the pulse is concerned, also providing a glimpse at birth and development of the FTI wave packets in time during the interval of the laser pulse duration.

C. Dependence of the time of birth on the pulse duration and the CEP

As one can see from Fig. 3, the FTI electrons tend to be released before the peaks of the electric field. This fact has been noted before [12] on the basis of the semiclassical CTMC analysis for the pulses with duration exceeding $N_c = 4$ OC. Our results for the multicycle pulses agree with the CTMC predictions. For the single cycle pulses with larger CEPs ($\phi = \pi/2$ and $3\pi/4$), shown in Fig. 1, the pattern is different, and FTI wave packets are born after the peaks of the electric field. We believe that this is an effect of the ultrashort pulse duration. To elucidate this question we performed a series of CTMC calculations. These calculations followed closely those reported in [12]; we will give, therefore, only a very brief description of the theoretical procedure we employed. To each electron's trajectory released at a particular moment t_0 with initial conditions $\boldsymbol{r}_0$ and $\boldsymbol{v}_0$, we ascribe a weight factor proportional to the Ammosov-Delone-Krainov (ADK) instantaneous ionization rate [40] $W(t_0, v_{0,\perp})$, where $v_{0,\perp}$ is the

TABLE I. Ratio R of the number of trajectories released before and after the main maximum of the laser pulse for different CEPs ϕ and pulse durations $T_1 = N_c T$. Peak field strength $E_0 = 0.0534$ a.u., base frequency $\omega = 0.057$ a.u.

ϕ	N_c	R
0	1	2.00
$\pi/4$	1	5.45
$\pi/2$	1	0.19
$3\pi/4$	1	0.64
0	2	3.40
0	3	2.83
0	4	1.71

velocity component perpendicular to the polarization direction. The parallel velocity component was, as is often assumed in the CTMC calculations, put to zero. The initial coordinates (x_0, y_0) in the perpendicular directions also had zero values, while z_0 was determined on the basis of the energy conservation law in parabolic coordinates as was done in [12]. Classical trajectories with these initial conditions are propagated in time in the combined field of the laser pulse and the soft-core atomic Coulomb potential. The trajectories having at the end of the pulse the electron's energies above the ground level and below the ionization threshold are considered as the FTI electron trajectories. We calculate the ratio R of the number of the trajectories (including the ADK weight factor) released before and after the main maximum of the laser pulse electric-field strength. The CTMC results thus obtained for the CEPs and N_c values used in the quantum TDSE calculations in Figs. 1 and 3 are summarized in Table I.

The CTMC results for the single cycle pulse in Table I reveal essentially the same pattern as the TDSE results shown in Fig. 1; for larger CEP values ($\phi = \pi/2$ and $3\pi/4$) FTI wave packets tend to be born after the peaks of the electric field. We checked that this effect is not very sensitive to the particular form of the atomic potential employed in the CTMC calculations and is, therefore, probably a consequence of the very short pulse duration.

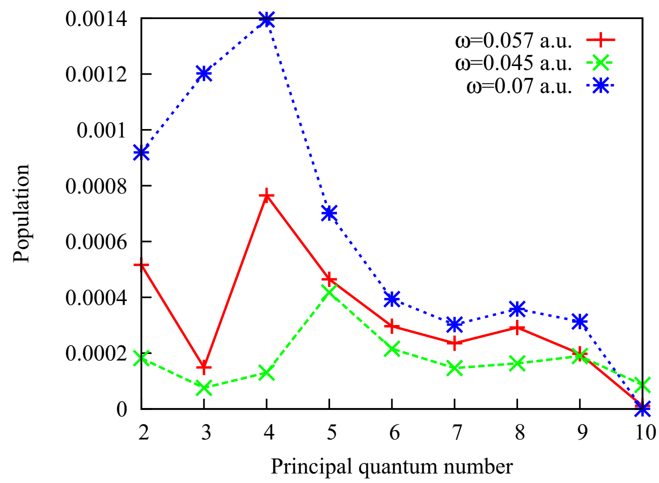

FIG. 6. Population of Rydberg levels for single cycle pulses with $E_0 = 0.0534$ a.u., $\phi = 0$, and different base frequencies ω.

D. Frequency dependence

In Fig. 5 we show correlation patterns we obtain changing the base frequency ω and keeping constant the peak field strength $E_0 = 0.0534$ a.u. and CEP value $\phi = 0$ for the driving pulse (1). Comparison of the results in Figs. 5 and 1(a) shows that the spatial size of the correlation pattern shrinks in the z direction with increasing frequency. This should lead to a corresponding decrease in population of the higher-lying Rydberg states after the end of the pulse. One can see from Fig. 6 that this is indeed the case. We show in this figure the Rydberg state population distributions obtained after the end of the pulse for these particular frequencies. This trend of the diminishing of the spatial extension of the FTI wave packets and the corresponding decrease of the popula-

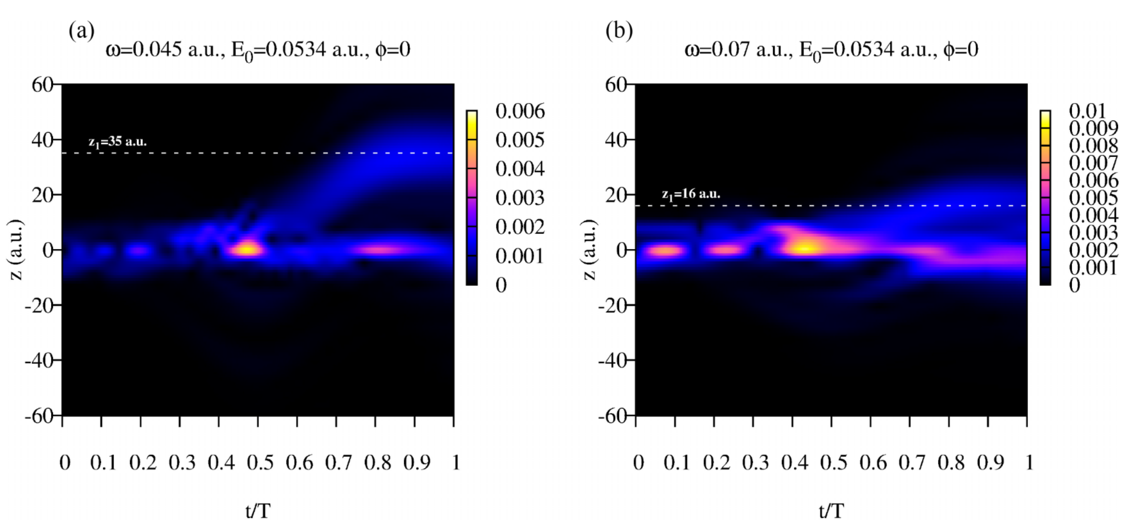

FIG. 5. Magnitudes $|\tilde{C}(z_0, t; \mathcal{R}, T_1)|$ of the normalized correlation function (8) for single cycle pulses with different base frequencies ω. Time is measured in units of an optical cycle $T = 2\pi/\omega$. White dashed lines show z coordinates of the crests of the FTI wave packets at the end of the pulse.

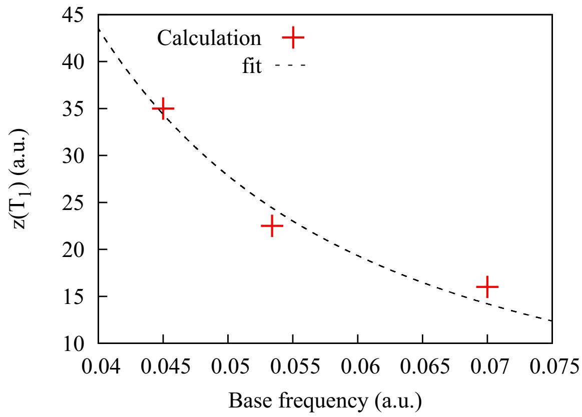

FIG. 7. z coordinates of the crests of the FTI wave packets at the end of the pulse: values from Figs. 1(a), 5(a), and 5(b) (crosses) and fit $z(T_1) = A/\omega^2$ (dashed line).

tion of the high-lying Rydberg states with growing frequency probably is, as was suggested in [2], a consequence of the diminishing of the electron excursion radius E_0/ω^2. The ionic Coulomb potential plays a very important role in the formation of the FTI, but the overall spatial scale of the electron motion is set by the electric field and it shrinks as the frequency increases. Figure 7 illustrates this statement. It shows estimates for $z(T_1)$, the z coordinate of the FTI wave-packet crest at the end of the pulse that we obtain from Figs. 1(a), 5(a), and 5(b). These estimates correspond to the peak strength $E_0 = 0.0534$ a.u. and base frequencies $\omega = 0.057$, 0.045, and 0.07 a.u., respectively. One can see from Fig. 7 that the $z(T_1)$ values we obtain from the correlation patterns in Figs. 1 and 5 agree reasonably well with the results given by a fitting formula: $z(T_1) = A/\omega^2$ with $A = 0.0691$.

IV. CONCLUSION

We presented a procedure allowing us to trace the past history of the FTI electrons ending up in the atomic Rydberg levels after the end of the driving laser pulse. The procedure is based on a computation of the correlation between the two observables: A and B. The observable A described the electron's detection in a Rydberg state at the end of the pulse. A projection operator on the manifold of the Rydberg levels was used to represent this observable. As an observable B we used the electron's coordinate at the moment of time t inside the laser pulse. The theoretical arguments we presented and the results of the numerical calculation show that the correlation function analysis for these two observables allows us to visualize the FTI process in detail. In particular, we were able to detect the moments of birth of the FTI electrons and see distinctly the spatial structure of atomic Rydberg levels populated by these electrons.

We performed such a correlation analysis for different driving pulse parameters, varying pulse CEP, frequency, and duration. The results we obtained generally agree with the previous semiclassical CTMC analysis [12], in particular regarding the role that the increasing pulse duration plays in populating the higher-lying Rydberg levels. Our procedure can, in fact, provide an important and useful ingredient for the CTMC calculations: the initial conditions which CTMC requires to propagate the trajectories in time. For the choice of the observable B we made in the present paper, the correlation analysis provides both the birth time of an FTI electron and its coordinate at the instant of birth. We note that observable B need not necessarily be the electron's coordinate. It can just as well be the electron's velocity, for example. Using our approach, we may, therefore, obtain information about the FTI electron's velocity at the birth moment. We plan to perform such an analysis of the FTI combining both present quantum-mechanical procedure and the semiclassical CTMC in the future.

As we mentioned above, we are not restricted in choosing the coordinate operator for the observable B in applications of our procedure. Nor are we obliged to use the projection operator on the manifold of the Rydberg levels to represent observable A. Our procedure is flexible enough to allow different choices of the observables suitable to study various ionization phenomena. In the works [23,24] we used a projection operator on the continuous spectrum of the field-free atomic Hamiltonian for the observable A. The observable A in this case is the event of atomic ionization and our procedure allows us to obtain a glimpse of the ionization dynamics. Other choices of A are possible. By adding the photon degrees of freedom to the problem which can be done using the numerical technique we described in [39], we may require A to represent a physical situation with an electron in a ground atomic state and an emitted harmonic photon. This choice would enable us to take a glimpse at the development of the HHG. We plan to perform such a calculation in the future.

ACKNOWLEDGMENTS

This work was supported by the Institute for Basic Science under Grant No. IBS-R012-D1. Computational works for this research were performed on the Institute for Basic Science (IBS) Supercomputer Aleph in the IBS Research Solution Center. I.A.I. wishes to thank the Australian National University for hospitality.

[1] M. Gavrila, J. Phys. B: At. Mol. Opt. Phys. **35**, R147 (2002).
[2] T. Nubbemeyer, K. Gorling, A. Saenz, U. Eichmann, and W. Sandner, Phys. Rev. Lett. **101**, 233001 (2008).
[3] U. Eichmann, T. Nubbemeyer, H. Rottke, and W. Sandner, Nature (London) **461**, 1261 (2009).
[4] N. I. Shvetsov-Shilovski, S. P. Goreslavski, S. V. Popruzhenko, and W. Becker, Laser Phys. **19**, 1550 (2009).
[5] E. A. Volkova, A. M. Popov, and O. V. Tikhonova, J. Exp. Theor. Phys. **113**, 394 (2011).
[6] H. Liu, Y. Liu, L. Fu, G. Xin, D. Ye, J. Liu, X. T. He, Y. Yang, X. Liu, Y. Deng *et al.*, Phys. Rev. Lett. **109**, 093001 (2012).
[7] A. S. Landsman, A. N. Pfeiffer, C. Hofmann, M. Smolarski, C. Cirelli, and U. Keller, New J. Phys. **15**, 013001 (2013).

[8] U. Eichmann, A. Saenz, S. Eilzer, T. Nubbemeyer, and W. Sandner, Phys. Rev. Lett. **110**, 203002 (2013).
[9] W.-H. Xiong, X.-R. Xiao, L.-Y. Peng, and Q. Gong, Phys. Rev. A **94**, 013417 (2016).
[10] H. Zimmermann, S. Patchkovskii, M. Ivanov, and U. Eichmann, Phys. Rev. Lett. **118**, 013003 (2017).
[11] J. Dubois, S. A. Berman, C. Chandre, and T. Uzer, Phys. Rev. Lett. **121**, 113202 (2018).
[12] L. Ortmann, C. Hofmann, I. A. Ivanov, and A. S. Landsman, Phys. Rev. A **103**, 063112 (2021).
[13] M. Liu, S. Xu, S. Hu, W. Becker, W. Quan, X. Liu, and J. Chen, Optica **8**, 765 (2021).
[14] M. Baker, A. J. Palmer, W. R. MacGillivray, and R. T. Sang, Nanotechnology **15**, 1356 (2004).
[15] Z.-T. Lu, P. Schlosser, W. Smethie, N. Sturchio, T. Fischer, B. Kennedy, R. Purtschert, J. Severinghaus, D. Solomon, T. Tanhua *et al.*, Earth-Sci. Rev. **138**, 196 (2014).
[16] A. Facon, E.-K. Dietsche, D. Grosso, S. Haroche, J.-M. Raimond, M. Brune, and S. Gleyzes, Nature (London) **535**, 262 (2016).
[17] B. Ohayon, J. Chocron, T. Hirsh, A. Glick-Magid, Y. Mishnayot, I. Mukul, H. Rahangdale, S. Vaintraub, O. Heber, D. Gazit *et al.*, Hyperfine Interact. **239**, 57 (2018).
[18] Y. Zhao, Y. Zhou, J. Liang, Z. Zeng, Q. Ke, Y. Liu, M. Li, and P. Lu, Opt. Express **27**, 21689 (2019).
[19] H. Yun, J. H. Mun, S. I. Hwang, S. B. Park, I. A. Ivanov, C. H. Nam, and K. T. Kim, Nat. Photonics **12**, 620 (2018).
[20] J. H. Mun, I. A. Ivanov, H. Yun, and K. T. Kim, Phys. Rev. A **98**, 063429 (2018).
[21] C. A. Brewer, F. Brizuela, P. Wachulak, D. H. Martz, W. Chao, E. H. Anderson, D. T. Attwood, A. V. Vinogradov, I. A. Artyukov, A. G. Ponomareko *et al.*, Opt. Lett. **33**, 518 (2008).
[22] J. Xu, Y. Zhou, Y. Li, A. Liu, Y. Chen, X. Ma, X. Huang, K. Liu, Q. Zhang, M. Li *et al.*, New J. Phys. **24**, 123043 (2022).
[23] I. Ivanov and K. T. Kim, J. Phys. B: At. Mol. Opt. Phys. **55**, 055001 (2022).
[24] I. Ivanov and K. T. Kim, Sci. Rep. **12**, 19533 (2022).
[25] S. V. Popruzhenko, J. Phys. B: At. Mol. Opt. Phys. **47**, 204001 (2014).
[26] E. J. Heller, J. Chem. Phys. **68**, 2066 (1978).
[27] E. J. Heller, Acc. Chem. Res. **14**, 368 (1981).
[28] V. Engel, Chem. Phys. Lett. **189**, 76 (1992).
[29] M. Praprotnik and D. Janežič, J. Chem. Phys. **122**, 174103 (2005).
[30] I. A. Ivanov, Phys. Rev. A **90**, 013418 (2014).
[31] I. A. Ivanov and A. S. Kheifets, Phys. Rev. A **87**, 033407 (2013).
[32] I. A. Ivanov, J. Dubau, and K. T. Kim, Phys. Rev. A **94**, 033405 (2016).
[33] M. Nurhuda and F. H. M. Faisal, Phys. Rev. A **60**, 3125 (1999).
[34] A. M. Steinberg, Phys. Rev. A **52**, 32 (1995).
[35] D. Sokolovski and J. N. L. Connor, Phys. Rev. A **44**, 1500 (1991).
[36] D. J. Miller, Nuovo Cimento B **112**, 1577 (1997).
[37] I. I. Hirschman and D. V. Widder, *The Convolution Transform* (Princeton University, Princeton, NJ, 1955).
[38] L. D. Landau and E. M. Lifshitz, *Quantum Mechanics* (Pergamon, New York, 1977).
[39] I. A. Ivanov and K. T. Kim, Sci. Rep. **11**, 3956 (2021).
[40] M. V. Ammosov, N. B. Delone and V. P. Krainov, Sov. Phys. JETP **64**, 1191 (1986).